https://doi.org/10.1016/j.jelechem.2021.115965

Hierarchical Mesoporous MoS_2 Frameworks with Conformal Carbon Coating as a High-Rate and Stable Anode in Li-Ion Battery

Kang Ding,[a] *Jeongyeon Lee,*[a] *Lawrence Yoon Suk Lee,*[a,b,]* *Kwok-Yin Wong*[a,]*

[a] Department of Applied Biology and Chemical Technology and the State Key Laboratory of Chemical Biology and Drug Discovery, The Hong Kong Polytechnic University, Hung Hom, Kowloon, Hong Kong SAR, China.

[b] Research Institute for Smart Energy, The Hong Kong Polytechnic University, Hung Hom, Kowloon, Hong Kong SAR, China.

* Corresponding authors: lawrence.ys.lee@polyu.edu.hk (L.Y.S. Lee); kwok-yin.wong@polyu.edu.hk (K.-Y. Wong)

Keywords: molybdenum sulfide; phase-segregation; nanocomposite; anode; lithium-ion battery

Abstract

Hierarchical or mesoporous-structured molybdenum disulfides (MoS_2) are one of the promising anode materials for lithium-ion batteries (LIBs) owing to their abundant active sites, fast ion transport, and easy permeation of electrolyte. However, the synthesis of such architectures with precise structural control is challenging, often requiring preliminary fabrication of templates or special equipment. Herein, we report hierarchical and mesoporous MoS_2 frameworks (HM-MoS_2) synthesized *via* a facile phase-segregation route, where ZnS nanoparticles are *in situ* formed as the hard template. The mesopores and interconnected channels created by removing ZnS nanoparticles enable the uniform carbon coating on HM-MoS_2. When employed as an anode in LIB, the HM-MoS_2 of an optimal carbon coating exhibits a high rate capability of 396.8 mA h g^{-1} at 10 A g^{-1} and a prolonged cyclability with only 2.8 % of capacity decay.

1. Introduction

The need for renewable energy has been rapidly increasing due to the deteriorating energy and environmental issues worldwide. The intermittent nature of renewable energy sources requires efficient energy storage devices to realize a continuous supply of electricity [1, 2]. Currently, lithium-ion batteries (LIBs) are leading the energy storage market, in particular, for portable electronic devices, owing to their high energy density, high efficiency, and long-term cyclability [3-5]. The application of LIBs is rapidly expanding to electrical vehicles and large-scale smart grids, which require improved LIB performances such as a higher energy density and faster-charging capability.

Graphite, a commercially available anode material in LIBs, bears a theoretical specific capacity of 372 mA h g^{-1} by forming LiC_6 [6]. Although graphite allows stable shuttling of Li^+ ions, it offers insufficient capacity per unit mass, which makes it difficult to meet the practical needs of power batteries. So far, extensive effort has been devoted to the development of superior anode materials that can provide higher capacity than graphite. Among the many candidates, molybdenum disulfide (MoS_2) has been identified as a promising low-cost anode material for LIBs. MoS_2 has a graphite-like layered architecture where the adjacent MoS_2 layers are held together by weak van der Waals force and thus the smooth diffusion of Li^+ is ensured [7]. MoS_2 also undergoes a conversion reaction: lithiated MoS_2 further reacts with Li^+ to form Li_2S and Mo at low voltages, delivering a theoretical capacity of *ca*. 670 mA h g^{-1} in the working voltage window [8]. Among the three common polymorphs of MoS_2, *i.e.*, 2H, 1T, and 3R MoS_2, 2H MoS_2 is thermodynamically stable and most widely used [9, 10]. Nevertheless, 2H MoS_2 is an intrinsic semiconductor with low electrical conductivity and as a result, exhibits low specific capacity and inferior rate performance. Moreover, MoS_2 suffers from capacity fading caused by the drastic volume variation and shuttling of polysulfides during the charging/discharging processes [11-13].

In an attempt to tackle these issues and realize the practical utilization of 2H MoS_2, several approaches have been explored, including the integration of MoS_2 into carbonaceous skeletons and the designing of nanostructured MoS_2. For instance, Yuan *et al*. used a drop-coating/freeze-drying strategy to anchor MoS_2/graphene hybrid aerogels on a carbon fiber paper and pyrolyzed them to obtain a binder-free electrode for LIBs [14]. The conductive 3D network and porous structure of this electrode facilitated the electron/ion transport and provided abundant active sites, which enabled superior electrochemical performance. Ru *et al*. also reported MoS_2/SnS hollow nanostructures that were constructed by a covalent assembly strategy. The integration of MoS_2 and SnS facilitated Li^+ diffusion and provided a mechanically robust framework during the charging/discharging processes, thereby achieving fast and stable lithium storage [15]. Among a variety of architectures, hierarchical and mesoporous structures have been frequently constructed to alleviate mechanical stress upon electrode deformation by creating abundant active sites to accommodate Li^+ and providing sufficient ion/electron transport pathways [16, 17]. In general, the fabrication of such hierarchical/mesoporous structures requires hard/soft templates such as SiO_2 nanoparticles [18], SBA-15 [17], and Sb_2S_3 microrods [19], which need an extra step for their pre-synthesis. Spraying synthesis is another route to prepare mesoporous materials without using templates, but specially-designed equipment is required [20].

In this work, we report the synthesis of hierarchical mesoporous MoS_2 (HM-MoS_2) frameworks *via* a phase-segregation route using $(NH_4)HZn_2(OH)_2(MoO_4)_2$ nanosheets as the precursor and their application as an anode for LIB. The solid–gas sulfidation of the precursor produces a hybrid composite of MoS_2/ZnS nanoparticles, and the ZnS nanoparticles serve as *in situ* formed hard template that can be easily removed to afford a porous structure. This approach ensures the integrity of the coral-like hierarchical MoS_2 nanosheet structure, creating a homogeneous distribution of pores. To such porous MoS_2 nanosheets, uniform carbon coating

was applied to improve the conductivity and structural stability. Polydopamine, which can adhere to a wide range of surfaces, was engaged as the carbon source and provided a nitrogen-doped carbon layer of controllable thickness *via* a facile immersion in dopamine solution [21]. The HM-MoS_2 with an optimal carbon coating (HM-MoS_2/C_{100}) exhibits good electrical conductivity and structural stability, and when used as an anode in LIB, it delivers superior rate capability and cyclability thanks to the fast ion transport during the lithiation/delithiation process.

2. Experimental Section

2.1. Chemicals

Ammonium heptamolybdate tetrahydrate ($(NH_4)_6Mo_7O_{24}\cdot 4H_2O$, AR) and tris(hydroxymethyl)aminomethane ($NH_2C(CH_2OH)_3$, 99 %) were purchased from Shenzhen Dieckmann Tech. Zinc nitrate hexahydrate ($Zn(NO_3)_2\cdot 6H_2O$, 98 %), sulfur powder (> 99.5 %), and dopamine hydrochloride ($(HO)_2C_6H_3(CH_2)_2NH_2\cdot HCl$. 98 %) were purchased from Sigma–Aldrich. Ammonium hydroxide solution ($NH_3\cdot H_2O$, 28 % in water) was purchased from Tokyo Chemical Industry. Hydrochloride acid (HCl, 35.0~37.0 %) and ethanol (≥ 99.9 %) were purchased from Duksan Pure Chemicals. All chemicals were used as received.

2.2. Synthesis of hierarchical mesoporous MoS_2 frameworks (HM-MoS_2)

$(NH_4)HZn_2(OH)_2(MoO_4)_2$ nanoplates, the precursor, were first prepared by a precipitation method according to a reported procedure with minor modifications [22]. Briefly, to an aqueous solution (200 mL) containing $(NH_4)_6Mo_7O_{24}\cdot 4H_2O$ (2 mmol) and $NH_3\cdot H_2O$ (28 %, 2.5 mL), an aqueous solution of $Zn(NO_3)_2\cdot 6H_2O$ (14 mmol, 100 mL) was added dropwise with stirring, and the mixture was stirred for 1.5 h at room temperature. The precipitated precursor was collected by centrifugation, washed with water and ethanol in sequence, and dried at 60 °C in an oven. The HM-MoS_2 was prepared by a gas–solid reaction in an argon atmosphere. The as-synthesized $(NH_4)HZn_2(OH)_2(MoO_4)_2$ precursors (130 mg) and sulfur powder (400 mg) were

placed in a dual heating zone tube furnace. Under the argon flow, the temperature was raised to 500 °C at a ramping rate of 10 °C min^{-1} and maintained for 2 h to afford a composite of MoS_2 and ZnS. After cooling to room temperature, the obtained composite was dispersed in 1 M HCl and stirred for 24 h to remove ZnS, filtered, and dried under vacuum at 50 °C overnight to yield the HM-MoS_2 frameworks.

2.3. Synthesis of carbon-coated HM-MoS_2 (HM-MoS_2/C) and B-MoS_2 (B-MoS_2/C)

To a water/ethanol mixed solution (vol. water/ethanol = 9/1) containing the as-prepared HM-MoS_2 (60 mg), tris(hydroxymethyl)aminomethane (121 mg), and a pre-determined amount of dopamine hydrochloride were added and stirred for 5 h at room temperature to polymerize the dopamine on the surface of HM-MoS_2. The polydopamine-coated HM-MoS_2 was washed with water, dried at 50 °C in a vacuum oven, and heated in a tube furnace at 700 °C in argon atmosphere for 2 h to yield the carbon-coated HM-MoS_2 (HM-MoS_2/C_X, where X denotes the amount of dopamine hydrochloride used). For example, HM-MoS_2/C_{100} was prepared using 100 mg of dopamine hydrochloride. For comparison, pristine MoS_2 (B-MoS_2) was prepared by direct sulfidation of the ground $(NH_4)_6Mo_7O_{24}{\cdot}4H_2O$ at 500 °C for 2 h under argon flow. The carbon-coated B-MoS_2 (B-MoS_2/C) was fabricated using the same procedure used for the HM-MoS_2/C, except HM-MoS_2 was replaced with B-MoS_2 in the fabrication.

2.3. Characterization of materials

The morphology and structure of the samples were characterized by a scanning electron microscope (SEM, Tescan VEGA3) and a field emission electron microscope (JEOL Model JEM-2100F). An X-ray diffractometer (Rigaku SmartLab 9kW Advance) was used to analyze the crystal structure of samples. Raman spectra were collected on a Renishaw Micro-Raman Spectroscopy System equipped with a 532-nm laser source. A thermogravimetric analyzer (TA Instruments, TGA5500) was used to determine the wt.% of carbon in the samples. Elemental analysis was conducted by X-ray photoelectron spectroscopy (XPS, Thermo Scientific Nexsa)

and elemental mapping was performed using an energy-dispersive X-ray spectrometer (EDX) attached to the field emission electron microscope. The BET surface area and pore size distribution were probed by a surface area and porosimetry system (Micromeritics, ASAP 2460).

2.4. Battery Cell Assembly

Active materials, super P (conducting agent), and polyvinylidene difluoride (PVDF, binder) were homogeneously mixed in *N*-methylpyrrolidone (NMP) by magnetic stirring with a mass ratio of active material:super P:PVDF = 7:2:1 to form a slurry to fabricate the working electrodes. The slurry was cast on a piece of copper foil using a doctor blade and dried at 60 °C in a vacuum oven overnight. The dried electrode was cut in a circle (d = 12 mm) and the actual amount of active material was determined as 0.5~0.7 mg cm^{-2}. The half cells were assembled using the as-prepared electrodes as the working electrodes, a separator (Celgard 2500), lithium foils as the counter electrode, and 1.0 M $LiPF_6$ in a mixed solvent of ethylene carbonate, dimethyl carbonates, and ethyl methyl carbonate (volume ratio = 1:1:1) as the electrolyte in a glovebox filled with argon.

2.5. Electrochemical Measurements

Various electrochemical tests, including galvanometric charging–discharging profile, rate and cycling performances, and cyclic voltammetry (CV) for the initial ten cycles (scan rate = 0.2 mV s^{-1}) of the half cells, were conducted on a WonATech battery cycler system (WBCS3000L) in a voltage range of 1 mV – 3 V (*vs*. Li/Li^+). Electrochemical impedance spectroscopy (EIS) was conducted using Princeton multichannel electrochemical station. The frequency range for the EIS tests was from 100 mHz to 100 kHz with an amplitude of 5 mV.

3. Results and Discussion

Scheme 1 illustrates the synthetic procedure of carbon-coated hierarchical mesoporous MoS_2 (HM-MoS_2/C) using $(NH_4)HZn_2(OH)_2(MoO_4)_2$ as the precursor. The sulfidation of the

precursor produces the phase-segregated MoS_2 and ZnS composite (MoS_2/ZnS). The subsequent etching with HCl and polydopamine treatment of MoS_2/ZnS remove the ZnS and yield the HM-MoS_2/C (see Experimental section for details). The scanning electron microscopic (SEM) and transmission electron microscopic (TEM) images of the precursor show a coral-like nanostructure with an average lateral size of *ca*. 2 μm, which is made of intersecting 2D nanosheets (**Figures S1a–c**). The X-ray diffraction (XRD) pattern of the precursor (**Figure S1d**) matches well with the reported $(NH_4)HZn_2(OH)_2(MoO_4)_2$ layered structure [23]. The coral-like nanosheet morphology of the precursor is well retained during the entire synthetic procedure, as revealed by the SEM images in **Figure S2**. The smooth surface of the precursor (**Figure S1b**), however, is roughened after the sulfidation (**Figure S2b**), but its thickness and size remain unchanged.

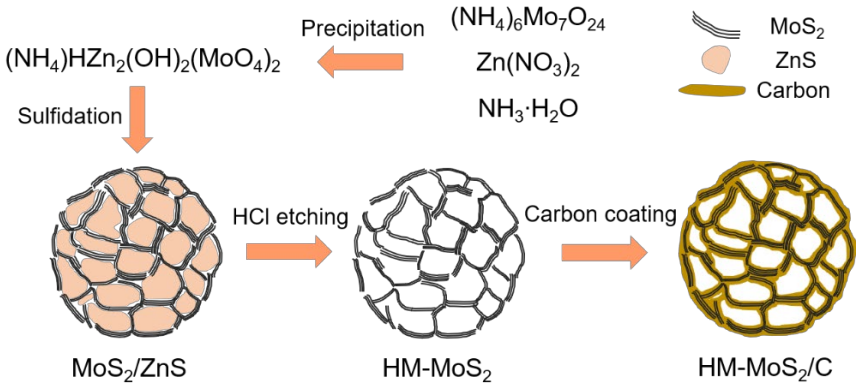

Scheme 1. Synthetic procedure of the HM-MoS_2/C.

The TEM images given in **Figure 1** provide a closer view of the structural evolution during the synthesis of HM-MoS_2/C_{100}. **Figures 1a** and **1b** are the TEM images of MoS_2/ZnS that reveal the embrace of ZnS nanoparticles by few-layer MoS_2 nanoflakes with a lateral size of *ca*. 20 nm. The small sizes of both ZnS and MoS_2 are attributed to the mutual restriction of their growths during the phase segregation. Two lattice fringes with interlayer distances of 0.314 and 0.624 nm are identified in the high-resolution TEM (HRTEM) image (**Figure 1c**), and they correspond to the (006) facet of wurtzite ZnS and the (002) plane of 2H MoS_2,

respectively. The HCl etching of MoS_2/ZnS removes the ZnS nanoparticles from the composite, leaving numerous pores and interconnected tunnels in the remaining MoS_2 frameworks (**Figures 1d – 1f**). After the polydopamine treatment, the HM-MoS_2/C_{100} displays homogeneous carbon layers (average thickness = *ca*. 3.7 nm) on the few-layer MoS_2 flakes (**Figures 1g – 1i**), the thickness of which varies from *ca*. 2 to 14 nm depending on the amount of dopamine hydrochloride used (**Figure S3**). The tap density of HM-MoS_2/C_{100} is determined as 0.6 g cm^{-3}. The elemental mapping images in **Figure 1j** confirm the homogeneous distribution of Mo and S atoms in HM-MoS_2/C_{100}.

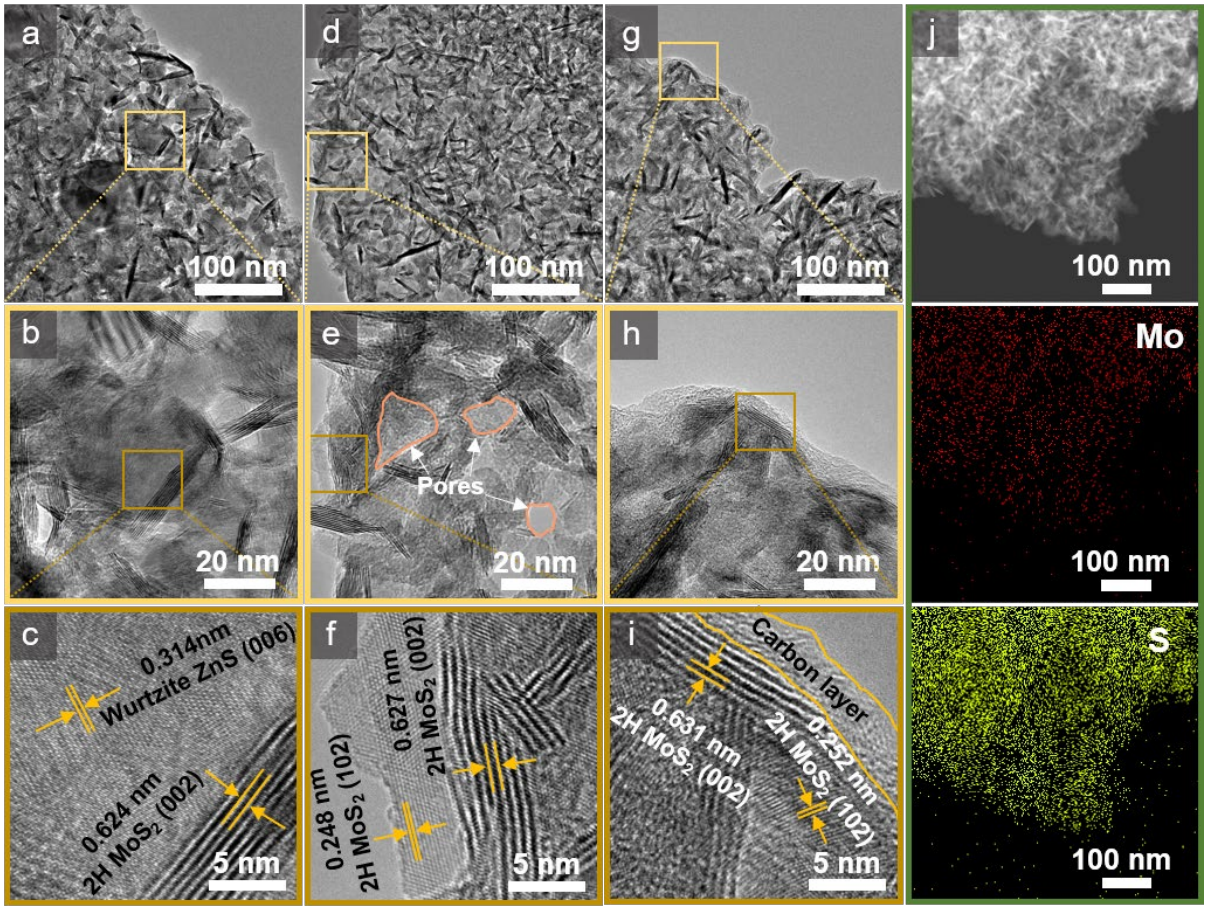

Figure 1. TEM and HRTEM images of (a–c) MoS_2/ZnS, (d–f) HM-MoS_2, and (g–i) HM-MoS_2/C_{100}. (j) Elemental mapping images of HM-MoS_2/C_{100}.

The ZnS nanoparticles that are *in situ* formed during the sulfidation of precursor act as the hard templates, which lead to the mesoporous morphology of HM-MoS_2/C. To investigate the effects of the unique structure of HM-MoS_2/C, pristine MoS_2 (B-MoS_2) was prepared by direct

sulfidation of $(NH_4)_6Mo_7O_{24}$ powder and coating with carbon (B-MoS_2/C) using the same method. In the absence of ZnS, the MoS_2 flakes aggregate to form bulk stacked nanoparticles with irregular shapes and sizes (**Figures S4** and **S5**), and a similar morphology is observed in B-MoS_2/C. Interestingly, B-MoS_2/C exhibits additional smaller (d = *ca*. 150 nm) nanospheres (**Figure S5a**), which are identified as amorphous carbon spheres formed during the carbonization. The formation of carbon nanospheres indicates that the surface area and pore structure of B-MoS_2 are unfavorable for the even and conformal coating of polydopamine, and thus the self-polymerization of dopamine without surface interaction with MoS_2 flakes is induced.

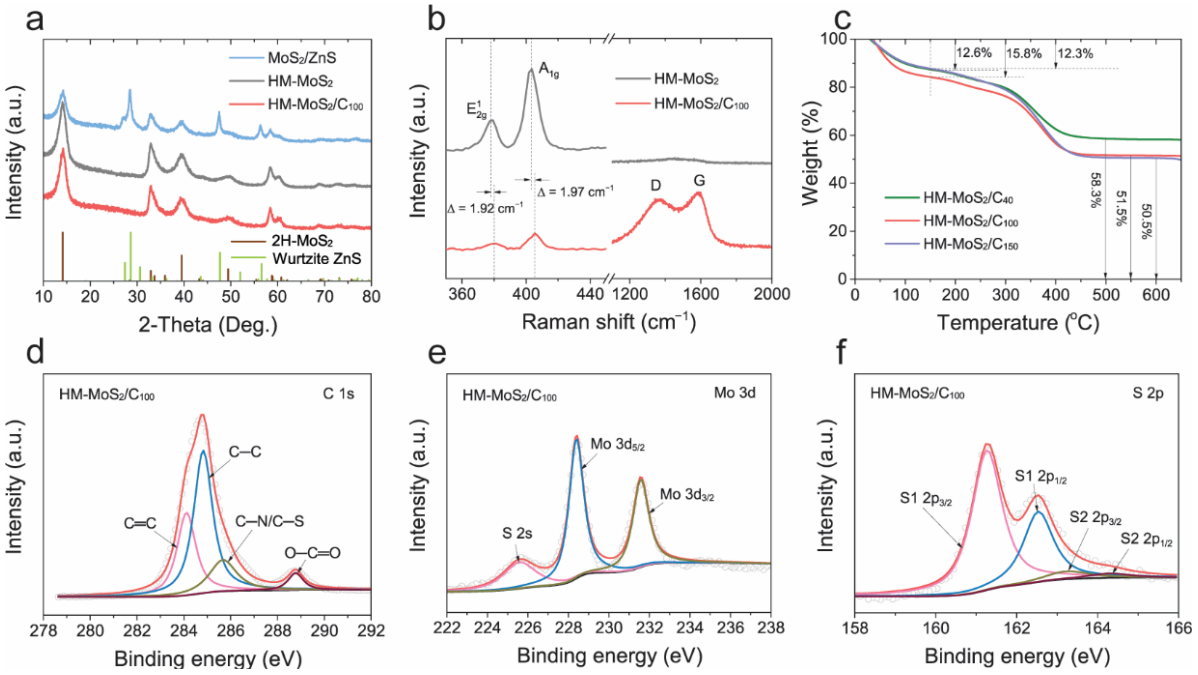

Figure 2. (a) XRD patterns of MoS_2/ZnS, HM-MoS_2, and HM-MoS_2/C_{100}. (b) Raman spectra of HM-MoS_2 and HM-MoS_2/C_{100}. (c) TGA curves of HM-MoS_2/C_{40}, HM-MoS_2/C_{100}, and HM-MoS_2/C_{150}. High-resolution XPS spectra of HM-MoS_2/C_{100} in (d) C 1s, (e) Mo 3d, and (f) S 2p regions.

Figure 2a compares the XRD patterns of MoS_2/ZnS, HM-MoS_2, and HM-MoS_2/C_{100}. MoS_2/ZnS clearly displays the characteristic dual phases of 2H MoS_2 (PDF No. 75-1539) and wurtzite ZnS (PDF No. 89-2739), while HM-MoS_2 and HM-MoS_2/C_{100} exhibit only the 2H MoS_2 phase, which confirms the removal of ZnS by HCl etching. B-MoS_2 and B-MoS_2/C also

show XRD peaks corresponding to the 2H MoS_2 phase (**Figure S6b**). Raman spectroscopy was engaged to get more insights into the structure of the samples (**Figures 2b** and **S7**). From all the samples, two Raman peaks are evident at *ca*. 382 and 407 cm^{-2}, which are correlated to the in-plane (E^1_{2g}) and out-of-plane (A_{1g}) vibrational modes of MoS_2, respectively [24]. Compared with those of HM-MoS_2, the E^1_{2g} and A_{1g} peaks of HM-MoS_2/C_{100} are blue-shifted by 1.92 and 1.97 cm^{-1}, respectively, due to the release of tensile strain upon annealing in argon atmosphere [25]. Similar peak shifts are observed from HM-MoS_2/C_{40} and HM-MoS_2/C_{150} (**Figure S7a**), as well as B-MoS_2/C (**Figure S7b**). It is worth noting that the E^1_{2g} and A_{1g} peaks of HM-MoS_2 are also significantly red-shifted (3.1 and 3.7 cm^{-1}, respectively) compared with those of B-MoS_2 (**Figures S7c**), which is most likely to be caused by the sulfur vacancies created during the acid removal of ZnS. [26, 27] The Raman signals of amorphous carbon are also detected from HM-MoS_2/C and B-MoS_2/C at *ca*. 1,362 (D band) and 1,586.8 cm^{-1} (G band), which indicate the disordered and graphitic carbon, respectively [28].

Thermogravimetric analyses (TGA) were conducted to measure the weight contents of carbon in the HM-MoS_2/C samples (**Figure 2c**). The initial weight loss at around 150 °C is due to the evaporation of adsorbed water, and the subsequent weight loss arises from the gradual oxidation of MoS_2 and carbon to MoO_3 and CO_2, respectively. Assuming that the weight % at 500 °C indicates the residual MoO_3, the carbon contents in HM-MoS_2/C_{40}, HM-MoS_2/C_{100}, and HM-MoS_2/C_{150} are determined as 25.8, 32.0, and 36.0 %, respectively (**Table S1**), which are in accordance with the amount of dopamine used for carbon coating. Meanwhile, the carbon content of B-MoS_2/C is much lower than those of the HM-MoS_2/C samples (18.2 %, **Figure S8**). This agrees with the TEM analyses that uncover the formation of carbon nanospheres as due to the limited surface area and unfavorable pore structure of B-MoS_2/C.

The surface area and pore size distribution of the samples were determined by Brunauer–Emmett–Teller (BET) and Barrett–Joyner–Halenda (BJH) analyses, respectively, and the

results are compared in **Figures S9** and **S10**. All the samples exhibit a typical IV-type isotherm featuring mesoporous adsorbents [29]. The pore size distribution curves, which are inversely proportional to the carbon content, indicate that the dominant pore size is decreased after the carbon coating. B-MoS_2 shows a narrower pore-size distribution with a smaller pore size (*ca*. 4 nm) than HM-MoS_2 (*ca*. 9 nm) as a result of its direct synthesis without the forming of a composite with ZnS. It is also obvious that the pore size distribution of B-MoS_2 remains unchanged after the carbon coating, which is an evidence that the pore structure of B-MoS_2 is unfavorable for the coating of the carbon layer. The BET surface areas and pore volumes of the samples are calculated and listed in **Table S2**. When coated with carbon, the BET surface area of HM-MoS_2 decreases from 146.1 to 87.5 $cm^2\ g^{-1}$ (HM-MoS_2/C_{40}) and it further drops to 70.6 (HM-MoS_2/C_{100}) and 70.7 $cm^2\ g^{-1}$ (HM-MoS_2/C_{150}) with thicker carbon coating. HM-MoS_2 mostly contains mesopores whose volume is calculated to be 0.382 $cm^3\ g^{-1}$. The carbon-coated samples also have mesopores as the dominant type, but they also possess small volumes of micropores. The volumes of mesopores in the HM-MoS_2/C samples decrease from 0.182 to 0.0853 $cm^3\ g^{-1}$ with increased carbon coating, whereas those of micropores slightly increase from 0.0064 to 0.0093 $cm^3\ g^{-1}$. B-MoS_2 has a much smaller surface area of 23.8 $cm^2\ g^{-1}$, which is further reduced to 15.2 $cm^2\ g^{-1}$ after carbon coating. The pore volumes of B-MoS_2 are also much smaller than those of the HM-MoS_2/C samples. The synthetic approach involving the ZnS template and phase segregation provides a simple yet effective route to achieving a high specific surface area and large pore volumes, even after carbon coating, which is beneficial for the permeation of electrolyte and transport of Li^+.

X-ray photoelectron spectroscopy (XPS) was engaged to probe the elemental composition and chemical states of the as-prepared samples. The survey spectra of the carbon-coated samples confirm the existence of S, Mo, C, N, and O without any impurities (**Figure S11**). The N signal is from the dopamine-derived carbon layer and is thus absent from HM-MoS_2. The

high-resolution C 1s spectrum of HM-MoS_2/C_{100} can be deconvoluted to four peaks at the binding energies of 284.1, 284.8, 285.7, and 288.8 eV, which are ascribed to the C=C, C–C, C–N/C–S, and O–C=O, respectively (**Figure 2d**) [30-33]. The Mo 3d spectrum exhibits two spin–orbit split peaks at 228.4 and 231.6 eV, which correspond to Mo^{4+} in MoS_2 (**Figure 2e**) [33, 34]. Other samples also show the same features of C 1s and Mo 3d spectra (**Figures S12** and **S13**). The S 2p spectrum of HM-MoS_2/C_{100} displays two sets of doublets (**Figure 2f**). The strong double peaks located at 161.3 (S $2p_{3/2}$) and 162.5 eV (S $2p_{1/2}$) can be attributed to the S^{2-} in MoS_2, while the other pair at 163.2 (S $2p_{3/2}$) and 164.3 eV (S $2p_{1/2}$) corresponds to the S 2p splitting peaks in C–S bond in the coated carbon [33, 35-37]. These S 2p splitting peaks intensify as carbon coating becomes thicker, which is in good agreement with the TGA and TEM analyses. Similarly, the pyridinic and pyrrolic N peaks in the N 1s spectra also increase with thicker carbon coating (**Figure S15**).

The effect of the hierarchical and porous structure of HM-MoS_2/C_{100} was investigated by evaluating the electrochemical behavior of Li-ion cells assembled using the as-prepared samples as the working electrode and Li foil as the counter electrode. **Figure 3a** shows the cyclic voltammograms (CVs) of the HM-MoS_2/C_{100} electrode recorded at a sweep rate of 0.2 mV s^{-1}. Two cathodic peaks appear at 0.89 and 0.34 V in the first scan, which can be ascribed to the intercalation of Li^+ into 2H-MoS_2, rendering a phase transformation to 1T Li_xMoS_2, and a conversion reaction from Li_xMoS_2 to metallic Mo and Li_2S, respectively [13, 17]. In the subsequent anodic scan, only one peak is observable at 2.35 V, which arises from the delithiation of Li_2S to form Li^+ and elemental S [13, 17]. From the second scan, a new cathodic peak appears at 1.91 V, which indicates the lithiation of the as-formed S to form Li_2S. As the scan proceeds, a small peak emerges at 2.1 V as a shoulder, which suggests the stepwise reduction of S as in the case of Li–S batteries [38]. The two cathodic peaks correlated to the Li^+ intercalation and conversion reaction are largely weakened and shifted to higher voltages.

In the reverse anodic process, an additional weak and broad peak is observed at 1.74 V, which corresponds to the partial oxidation of metallic Mo to MoS_2 [13, 17, 39].

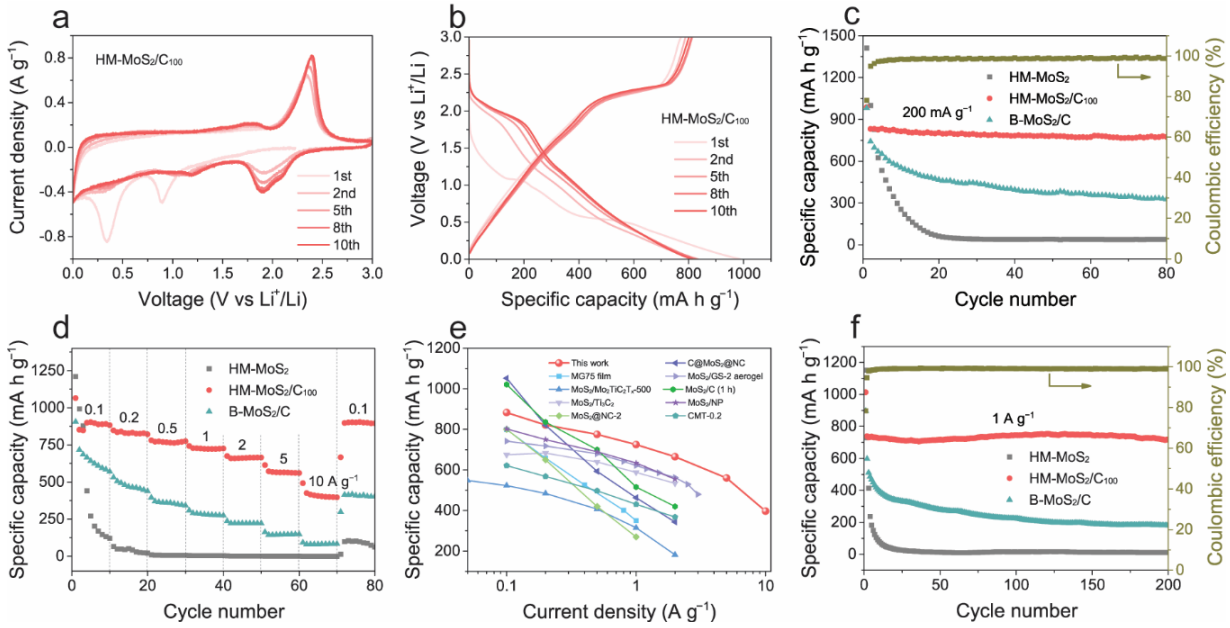

Figure 3. (a) CVs and (b) galvanostatic charge–discharge profiles of HM-MoS_2/C_{100}. (c) Cycling and (d) rate performances of HM-MoS_2, HM-MoS_2/C_{100}, and B-MoS_2/C. Cycling performance was tested at 200 mA g^{-1}. (e) Comparison of rate capability of HM-MoS_2/C_{100} with the recently reported MoS_2-based anodes for LIBs. (f) Long-term cycling performance of HM-MoS_2, HM-MoS_2/C_{100}, and B-MoS_2/C at 1 A g^{-1}.

Figure 3b is the galvanostatic charge–discharge profile of the HM-MoS_2/C_{100} electrode in a voltage range between 1 mV and 3 V (*vs*. Li^+/Li). The initial charge–discharge profile at a current density of 200 mA g^{-1} indicates the discharge and charge specific capacity of 987.9 and 772.6 mA h g^{-1}, respectively. The initial Coulombic efficiency (CE) is calculated as 78.2 %, which is higher than that of HM-MoS_2 (72.6 %) and B-MoS_2/C (76.4 %). In the subsequent discharge–charge cycles at 200 mA g^{-1}, the capacity values slightly increase due to the electrochemical activation of active materials [40], and stabilize at the 8th cycle, indicating good cycle stability. On the contrary, HM-MoS_2 and B-MoS_2/C suffer from cycle instability, showing a considerable drop in capacity (**Figure S16**). The cycling tests performed at 200 mA g^{-1} further confirm the stability enhancement of HM-MoS_2/C_{100} (**Figure 3c**). During the first

20 cycles, the HM-MoS_2/C_{100} electrode delivers stable performance, showing almost no capacity loss, whereas the B-MoS_2/C and HM-MoS_2 electrodes show considerable capacity decays. At the end of the 80th cycle, HM-MoS_2/C_{100} still maintains a specific discharge capacity of 773.6 mA h g^{-1} with a CE close to 100 %, which is a much better performance than B-MoS_2/C (327.2 mA h g^{-1}) and HM-MoS_2 (40.1 mA h g^{-1}). In the rate performance test, HM-MoS_2/C_{100} achieves specific capacities of 882.7, 821.5, 774.9, 725.2, 665.4, 560.2, and 396.8 mA h g^{-1} at 0.1, 0.2, 0.5, 1, 2, 5, and 10 A g^{-1}, respectively (**Figure 3d**). Upon returning to 0.1 A g^{-1}, the HM-MoS_2/C_{100} electrode recovers a specific capacity of 894.6 mA h g^{-1}, which indicates good reversibility of the redox reaction. HM-MoS_2/C_{100} displays a better rate capability than B-MoS_2/C and HM-MoS_2 at any current density. It is worth noting that HM-MoS_2/C_{40} with thinner carbon coatings shows larger capacities than HM-MoS_2/C_{100} and HM-MoS_2/C_{150} electrodes at current densities lower than 1 A g^{-1} (**Figure S17b**). However, it experiences a huge capacity decay at 2 A g^{-1} and delivers almost no capacity at 10 A g^{-1} in contrast to the stable performances of HM-MoS_2/C_{100} and HM-MoS_2/C_{150}. The carbon coating reduces the practical specific capacity of the HM-MoS_2/C electrodes, yet contributes to the higher-rate capability. The HM-MoS_2/C_{100} electrode with an optimal carbon coating thickness delivers good electrochemical performance, which is superior to most of the recently reported MoS_2-based anodes (**Figure 3e**) [12, 41-48]. The long-term cycling performances of the as-prepared electrodes at a current density of 1 A g^{-1} (the first cycle is at 100 mA g^{-1}) are compared in **Figure 3f**. The HM-MoS_2/C_{100} electrode demonstrates superior properties with stable cyclability, as evidenced by 97.2 % capacity retention (717.4 mA h g^{-1}) with a CE of 99.0 % after 200 cycles. The superior electrochemical performance of HM-MoS_2/C_{100} can be ascribed to the following reasons: 1) the hierarchical structure provides a large surface area and exposes abundant active sites to accommodate Li^+ to improve the specific capacity, 2) a large portion of mesopores within the frameworks promotes electrolyte permeation and ion diffusion,

strengthening fast charge/discharge behavior, 3) conformal carbon coating with optimal carbon thickness ensures good electrical conductivity and structural integrity upon prolonged cycling.

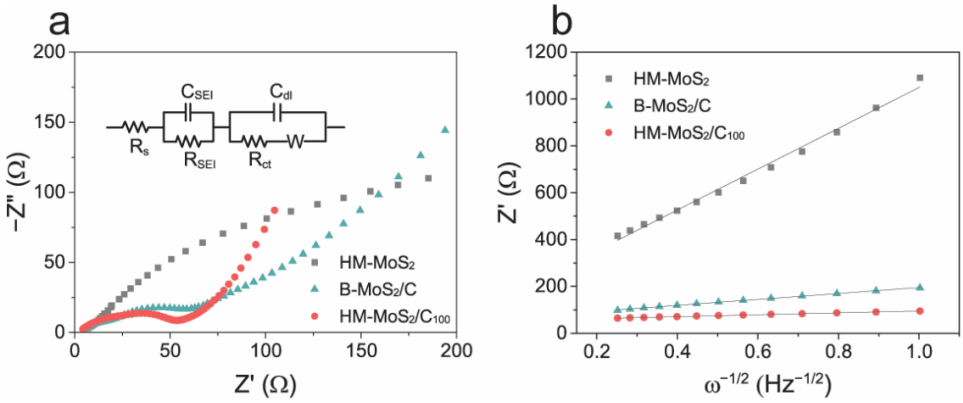

Figure 4. (a) Nyquist plots and (b) the corresponding Z' values plotted against $\omega^{-1/2}$ of half-cells fabricated with HM-MoS_2, HM-MoS_2/C_{100}, and B-MoS_2/C after 50 cycles at 1 A g^{-1}.

To understand the difference in electrochemical performance, electrochemical impedance spectroscopy (EIS) was carried out with the cycled electrodes (50 cycles at 1 A g^{-1}, **Figures 4** and **S18**). The Nyquist plots of HM-MoS_2/C_{100}, HM-MoS_2, and B-MoS_2 half-cells (**Figure 4a**) were fitted with the equivalent circuit (inset in **Figure 4a**), and the obtained parameters are listed in **Table S3**. All three cells possess similar internal resistances (R_s: 4.6 ~ 7.0 Ω) and resistance across the solid electrolyte interphase (SEI) layer (R_{SEI}: 10.1 ~ 13.7 Ω). However, the HM-MoS_2/C_{100} cell shows a much smaller charge transfer resistance (R_{ct}) value of 30.2 Ω than HM-MoS_2 (121.9 Ω) and B-MoS_2/C (35.2 Ω). Moreover, the linear tail in the low-frequency region indicates the Warburg impedance (Z_w), which is correlated with the diffusion process of Li^+ in the active materials. The diffusion coefficient of Li^+ (D_{Li^+}) within the electrode can be quantitatively determined based on the following equations [49]:

$$D_{Li^+} = \frac{R^2T^2}{2n^4F^4C^2\sigma^2A^2} \quad (1)$$

$$Z' = R_s + R_{ct} + \sigma\omega^{-\frac{1}{2}} \quad (2)$$

where R, F, and T represent the ideal gas constant, Faraday's constant, and absolute temperature, respectively; n is the number of electrons per molecule involved in the charge

transfer reaction; C is the concentration of Li^+; A is the surface area of the electrode; and σ is the Warburg factor which can be obtained by plotting the real resistance (Z') against the inverse square root of angular frequency ($\omega^{-1/2}$) at the linear region in the Nyquist plot and calculating the slope from the fitted line (**Figure 4b**) [49, 50]. The values of σ for HM-MoS_2/C_{100}, HM-MoS_2, and B-MoS_2/C are determined as 40.2, 871.5, 126.6 Ω $Hz^{1/2}$, respectively (**Table S3**). According to equation (1), a smaller Warburg factor of HM-MoS_2/C_{100} implies a larger Li^+ diffusion coefficient, thereby it provides the minimum resistance of Li^+ diffusion among the three materials. HM-MoS_2/C_{100} shows enhanced D_{Li^+} over HM-MoS_2 and B-MoS_2/C by 470.0 and 9.9, respectively. (see **Appendix** in the Supplementary Information)

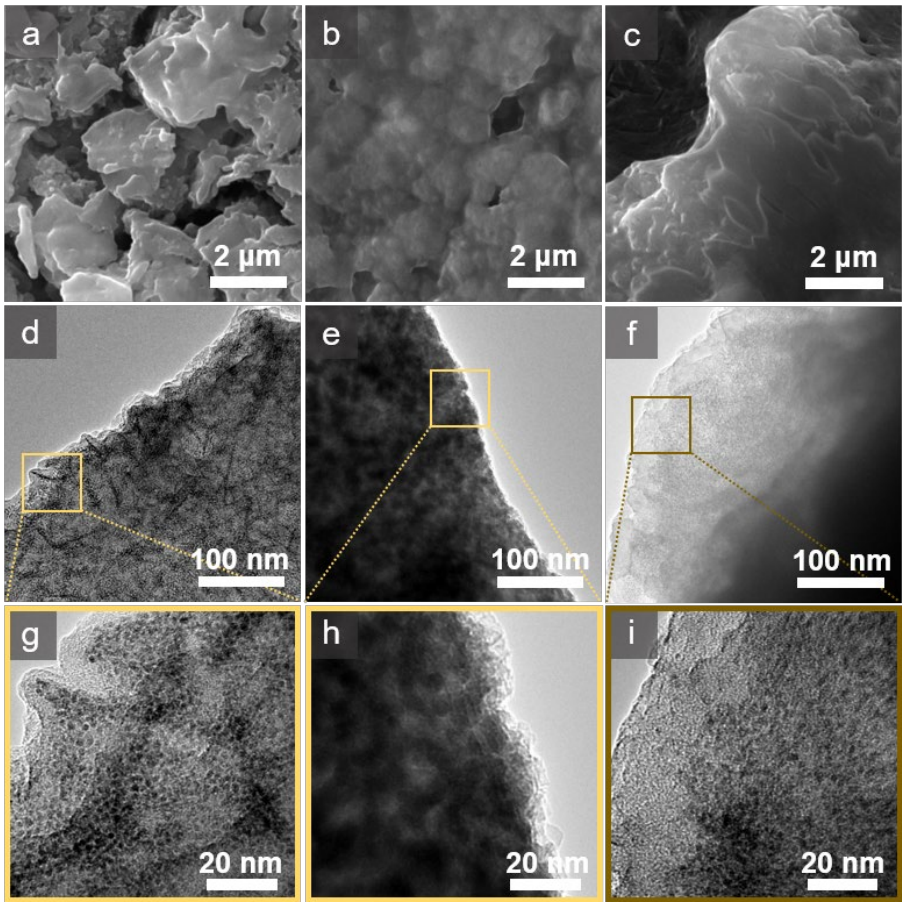

Figure 5. SEM (top panels) and TEM images (middle and bottom panels) of (a, d, g) HM-MoS_2/C_{100}, (b, e, h) HM-MoS_2, and (c, f, i) B-MoS_2/C after 50 cycles at 1 A g^{-1}.

Figure 5 displays the SEM and TEM images of the cycled electrodes. The SEM images of HM-MoS_2/C_{100}, HM-MoS_2, and B-MoS_2/C electrodes (**Figures 5a–c**) indicate that HM-

MoS_2/C_{100} still retains its sheet-like morphology, while HM-MoS_2 and B-MoS_2/C show severely aggregated morphology, which demonstrates that the carbon coating can prevent the morphological change. From the TEM images (**Figures 5e–i**), it is evident that the original MoS_2 flakes in HM-MoS_2/C_{100} are changed into tiny particles encapsulated by an amorphous carbon shell, while those in HM-MoS_2 are aggregated to small particles. The TEM images of B-MoS_2/C also indicate the disappearance of the original flaky structure. Without the protection of the carbon layer, HM-MoS_2 undergoes an extreme structural change and aggregation, which suggests a typical conversion reaction process. The carbon coating in HM-MoS_2/C_{100} effectively restricts such conversion process of the MoS_2 flakes, preventing the overgrowth of particles, and thus the hierarchical mesoporous structure remains undamaged. This enables the stable and prolonged cycles of HM-MoS_2/C_{100} electrode by pertaining the electrolyte permeation, Li^+ transport, as well as electrical conductivity.

4. Conclusions

In summary, a novel phase segregation route involving *in situ* formation of ZnS nanoparticles as the hard template was demonstrated to realize the hierarchical mesoporous MoS_2 frameworks. The interconnected channels and favorable pore structures of the obtained MoS_2 frameworks allow uniform carbon coating that endows the merits of efficient electrical conductivity, fast ion transport, easy permeation of electrolytes, and resistance to structural deterioration upon cycling. When applied as an anode in LIB, HM-MoS_2/C_{100} exhibits superior rate capability and good cycling stability as evidenced by a high specific capacity of 396.8 mA h g^{-1} at 10 A g^{-1} compared with HM-MoS_2 and B-MoS_2/C. After 200 cycles at 1 A g^{-1}, the HM-MoS_2/C_{100} electrode delivers a specific capacity of 717.4 mA h g^{-1} with almost no capacity decay. EIS data reveal that the cycled HM-MoS_2/C_{100} has the smallest charge transfer resistance and largest Li^+ diffusion coefficient compared with HM-MoS_2 and B-MoS_2/C. The post-cycle TEM images verify that the HM-MoS_2/C_{100} effectively retains a hierarchical

mesoporous architecture owing to the optimized carbon shells that act as a protective and conductive layer for high rate performance and stable cyclability.

Acknowledgement

We acknowledge the support from the Innovation and Technology Commission and The Hong Kong Polytechnic University. LYSL acknowledges the support from the Research Institute for Smart Energy. KYW acknowledges the support from the Patrick S. C. Poon Endowed Professorship.

References

[1] N. Xu, X. Li, X. Zhao, J.B. Goodenough, K. Huang, A novel solid oxide redox flow battery for grid energy storage, Energy Environ. Sci. 4 (2011) 4942-4946.

[2] Y. Lu, L. Yu, X.W. Lou, Nanostructured conversion-type anode materials for advanced lithium-ion batteries, Chem 4 (2018) 972-996.

[3] X. Li, X. Sun, X. Hu, F. Fan, S. Cai, C. Zheng, G.D. Stucky, Review on comprehending and enhancing the initial coulombic efficiency of anode materials in lithium-ion/sodium-ion batteries, Nano Energy 77 (2020) 105143.

[4] T.-F. Yi, H.M.K. Sari, X. Li, F. Wang, Y.-R. Zhu, J. Hu, J. Zhang, X. Li, A review of niobium oxides based nanocomposites for lithium-ion batteries, sodium-ion batteries and supercapacitors, Nano Energy 85 (2021) 105955.

[5] R. Xiong, Y. Pan, W. Shen, H. Li, F. Sun, Lithium-ion battery aging mechanisms and diagnosis method for automotive applications: recent advances and perspectives, Renewable Sustainable Energy Rev. 131 (2020) 110048.

[6] C. Yang, X. Zhang, J. Li, J. Ma, L. Xu, J. Yang, S. Liu, S. Fang, Y. Li, X. Sun, X. Yang, F. Pan, J. Lu, D. Yu, Holey graphite: A promising anode material with ultrahigh storage for lithium-ion battery, Electrochim. Acta 346 (2020) 136244.

[7] H. Sun, J.-G. Wang, W. Hua, J. Wang, D. Nan, B. Guo, Hierarchical MoS_2/N-doped carbon nanobelts assembled by interlaced nanosheets as high performance Li-ion battery anode, J. Alloys Compd. 821 (2020) 153339.

[8] Y. Jiao, A. Mukhopadhyay, Y. Ma, L. Yang, A.M. Hafez, H. Zhu, Ion transport nanotube assembled with vertically aligned metallic MoS_2 for high rate lithium-ion batteries, Adv. Energy Mater. 8 (2018) 1702779.

[9] Y. Guo, D. Sun, B. Ouyang, A. Raja, J. Song, T.F. Heinz, L.E. Brus, Probing the dynamics of the metallic-to-semiconducting structural phase transformation in MoS_2 crystals, Nano Lett. 15 (2015) 5081-5088.

[10] R.J. Toh, Z. Sofer, J. Luxa, D. Sedmidubský, M. Pumera, 3R phase of MoS_2 and WS_2 outperforms the corresponding 2H phase for hydrogen evolution, Chem. Commun. 53 (2017) 3054-3057.

[11] P. Wang, S. Sun, Y. Jiang, Q. Cai, Y.-H. Zhang, L. Zhou, S. Fang, J. Liu, Y. Yu, Hierarchical microtubes constructed by MoS_2 nanosheets with enhanced sodium storage performance, ACS Nano 14 (2020) 15577-15586.

[12] C. Chen, X. Xie, B. Anasori, A. Sarycheva, T. Makaryan, M. Zhao, P. Urbankowski, L. Miao, J. Jiang, Y. Gogotsi, MoS_2-on-MXene heterostructures as highly reversible anode materials for lithium-ion batteries, Angew. Chem., Int. Ed. 57 (2018) 1846-1850.

[13] H. Jiang, D. Ren, H. Wang, Y. Hu, S. Guo, H. Yuan, P. Hu, L. Zhang, C. Li, 2D monolayer MoS_2–carbon interoverlapped superstructure: engineering ideal atomic interface for lithium ion storage, Adv. Mater. 27 (2015) 3687-3695.

[14] J. Yuan, J. Zhu, R. Wang, Y. Deng, S. Zhang, C. Yao, Y. Li, X. Li, C. Xu, 3D few-layered MoS_2/graphene hybrid aerogels on carbon fiber papers: a free-standing electrode for high-performance lithium/sodium-ion batteries, Chem. Eng. J. 398 (2020) 125592.

[15] J. Ru, T. He, B. Chen, Y. Feng, L. Zu, Z. Wang, Q. Zhang, T. Hao, R. Meng, R. Che, Covalent assembly of MoS_2 nanosheets with SnS nanodots as linkages for lithium/sodium-ion batteries, Angew. Chem. 132 (2020) 14729-14735.

[16] L. Yang, S. Wang, J. Mao, J. Deng, Q. Gao, Y. Tang, O.G. Schmidt, Hierarchical MoS_2/polyaniline nanowires with excellent electrochemical performance for lithium-ion batteries, Adv. Mater. 25 (2013) 1180-1184.

[17] X. Fang, X. Yu, S. Liao, Y. Shi, Y.-S. Hu, Z. Wang, G.D. Stucky, L. Chen, Lithium storage performance in ordered mesoporous MoS_2 electrode material, Microporous Mesoporous Mater. 151 (2012) 418-423.

[18] M. Huang, H. Chen, J. He, B. An, L. Sun, Y. Li, X. Ren, L. Deng, P. Zhang, Ultra small few layer MoS_2 embedded into three-dimensional macro-micro-mesoporous carbon as a high performance lithium ion batteries anode with superior lithium storage capacity, Electrochim. Acta 317 (2019) 638-647.

[19] Q. Pan, Q. Zhang, F. Zheng, Y. Liu, Y. Li, X. Ou, X. Xiong, C. Yang, M. Liu, Construction of MoS_2/C hierarchical tubular heterostructures for high-performance sodium ion batteries, ACS Nano 12 (2018) 12578-12586.

[20] Y. Lu, Q. Zhao, N. Zhang, K. Lei, F. Li, J. Chen, Facile spraying synthesis and high-performance sodium storage of mesoporous MoS_2/C microspheres, Adv. Funct. Mater. 26 (2016) 911-918.

[21] J. Kong, W.A. Yee, L. Yang, Y. Wei, S.L. Phua, H.G. Ong, J.M. Ang, X. Li, X. Lu, Highly electrically conductive layered carbon derived from polydopamine and its functions in SnO_2-based lithium ion battery anodes, Chem. Commun. 48 (2012) 10316-10318.
[22] C. Peng, L. Gao, S. Yang, J. Sun, A general precipitation strategy for large-scale synthesis of molybdate nanostructures, Chem. Commun. (2008) 5601-5603.
[23] D. Levin, S.L. Soled, J.Y. Ying, Chimie douce synthesis of a layered ammonium zinc molybdate, Chem. Mater. 8 (1996) 836-843.
[24] L. Liang, V. Meunier, First-principles Raman spectra of MoS_2, WS_2 and their heterostructures, Nanoscale 6 (2014) 5394-5401.
[25] G. Kogo, B. Xiao, S. Danquah, H. Lee, J. Niyogushima, K. Yarbrough, A. Candadai, A. Marconnet, S.K. Pradhan, M. Bahoura, A thin film efficient pn-junction thermoelectric device fabricated by self-align shadow mask, Sci. Rep. 10 (2020) 1067.
[26] X. Wang, Y. Zhang, H. Si, Q. Zhang, J. Wu, L. Gao, X. Wei, Y. Sun, Q. Liao, Z. Zhang, K. Ammarah, L. Gu, Z. Kang, Y. Zhang, Single-atom vacancy defect to trigger high-efficiency hydrogen evolution of MoS_2, J. Am. Chem. Soc. 142 (2020) 4298-4308.
[27] Y. Li, S. Zuo, Q.-H. Li, X. Wu, J. Zhang, H. Zhang, J. Zhang, Vertically Aligned MoS_2 with In-Plane Selectively Cleaved Mo–S Bond for Hydrogen Production, Nano Lett. 21 (2021) 1848-1855.
[28] H. Lim, H. Kim, S.-O. Kim, W. Choi, Self-assembled N-doped MoS_2/carbon spheres by naturally occurring acid-catalyzed reaction for improved sodium-ion batteries, Chem. Eng. J. 387 (2020) 124144.
[29] M. Thommes, K. Kaneko, A.V. Neimark, J.P. Olivier, F. Rodriguez-Reinoso, J. Rouquerol, K.S.W. Sing, Physisorption of gases, with special reference to the evaluation of surface area and pore size distribution (IUPAC Technical Report), Pure Appl. Chem. 87 (2015) 1051-1069.
[30] S.A. Rakha, C. Jianqing, X. Huihao, Y. Guojun, D. Zhu, J. Gong, Incorporation of hydrogen in diamond thin films, Diamond Relat. Mater. 18 (2009) 1247-1252.
[31] Z. Pu, C. Zhang, I.S. Amiinu, W. Li, L. Wu, S. Mu, General strategy for the synthesis of transition-metal phosphide/N-doped carbon frameworks for hydrogen and oxygen evolution, ACS Appl. Mater. Interfaces 9 (2017) 16187-16193.
[32] Y. Ding, N. Huang, S. Yan, R. Peng, P. Sun, X. Sun, C. Huang, A MoS_2/sulfur-doped carbon sphere nanohybrid catalyst with high-efficiency electrocatalysis for flexible counter electrodes, J. Alloys Compd. 767 (2018) 848-855.

[33] Y. Zhang, H. Zhou, H. Wang, Y. Zhang, D.D. Dionysiou, Synergistic effect of reduced graphene oxide and near-infrared light on MoS_2-mediated electrocatalytic hydrogen evolution, Chem. Eng. J. 418 (2021) 129343.
[34] E. Koh, Y.T. Lee, Hybrid nanocomposites of a molybdenum disulfide (MoS_2) based hydrophobic filler for a robust self-cleaning effect, J. Ind. Eng. Chem. 96 (2021) 294-306.
[35] H. Liu, H. Hu, J. Wang, P. Niehoff, X. He, E. Paillard, D. Eder, M. Winter, J. Li, Hierarchical ternary MoO_2/MoS_2/heteroatom-doped carbon hybrid materials for high-performance lithium-ion storage, ChemElectroChem 3 (2016) 922-932.
[36] C. Wu, Y. Zhang, D. Dong, H. Xie, J. Li, Co_9S_8 nanoparticles anchored on nitrogen and sulfur dual-doped carbon nanosheets as highly efficient bifunctional electrocatalyst for oxygen evolution and reduction reactions, Nanoscale 9 (2017) 12432-12440.
[37] Y. Yao, Y. Guo, W. Du, X. Tong, X. Zhang, In situ synthesis of sulfur-doped graphene quantum dots decorated carbon nanoparticles hybrid as metal-free electrocatalyst for oxygen reduction reaction, J. Mater. Sci.: Mater. Electron. 29 (2018) 17695-17705.
[38] J. Lee, H. Song, K.-A. Min, Q. Guo, D. Kim, Z. Zheng, B. Han, Y. Jung, L.Y.S. Lee, Laser-ablated red phosphorus on carbon nanotube film for accelerating polysulfide conversion toward high-performance and flexible lithium–sulfur batteries, Small Methods 5 (2021) 2100215.
[39] B. Chen, Y. Meng, F. He, E. Liu, C. Shi, C. He, L. Ma, Q. Li, J. Li, N. Zhao, Thermal decomposition-reduced layer-by-layer nitrogen-doped graphene/MoS_2/nitrogen-doped graphene heterostructure for promising lithium-ion batteries, Nano Energy 41 (2017) 154-163.
[40] R. Wang, C. Xu, J. Sun, Y. Liu, L. Gao, H. Yao, C. Lin, Heat-induced formation of porous and free-standing MoS_2/GS hybrid electrodes for binder-free and ultralong-life lithium ion batteries, Nano Energy 8 (2014) 183-195.
[41] Y. Chao, R. Jalili, Y. Ge, C. Wang, T. Zheng, K. Shu, G.G. Wallace, Self-assembly of flexible free-standing 3D porous MoS_2-reduced graphene oxide structure for high-performance lithium-ion batteries, Adv. Funct. Mater. 27 (2017) 1700234.
[42] F. Wang, F. Li, L. Ma, M. Zheng, Few-layer MoS_2 nanosheets encapsulated in N-doped carbon hollow spheres as long-life anode materials for lithium-ion batteries, Chem. Eur. J. 25 (2019) 14598-14603.
[43] Z. Hu, X. Kuai, J. Chen, P. Sun, Q. Zhang, H.-H. Wu, L. Zhang, Strongly coupled MoS_2 nanocrystal/Ti_3C_2 nanosheet hybrids enable high-capacity lithium-ion storage, ChemSusChem 13 (2020) 1485-1490.

[44] S. Wang, R. Wang, Q. Zhao, L. Ren, J. Wen, J. Chang, X. Fang, N. Hu, C. Xu, Freeze-drying induced self-assembly approach for scalable constructing MoS_2/graphene hybrid aerogels for lithium-ion batteries, J. Colloid Interface Sci. 544 (2019) 37-45.
[45] H. Xue, S. Yue, J. Wang, Y. Zhao, Q. Li, M. Yin, S. Wang, C. Feng, Q. Wu, H. Li, D. Shi, Q. Jiao, MoS_2 microsphere@N-doped carbon composites as high performance anode materials for lithium-ion batteries, J. Electroanal. Chem. 840 (2019) 230-236.
[46] G. Zhao, Y. Cheng, P. Sun, W. Ma, S. Hao, X. Wang, X. Xu, Q. Xu, M. Liu, Biocarbon based template synthesis of uniform lamellar MoS_2 nanoflowers with excellent energy storage performance in lithium-ion battery and supercapacitors, Electrochim. Acta 331 (2020) 135262.
[47] Y.-H. Zhang, R.-H. Liu, L.-J. Zhao, L.-J. Xu, S.-H. Luo, Q. Wang, X. Liu, A large area mesh-like MoS_2 with an expanded interlayer distance synthesized by one-pot method and lithium storage performance, J. Electroanal. Chem. 873 (2020) 114428.
[48] J. Li, L. Han, X. Zhang, H. Sun, X. Liu, T. Lu, Y. Yao, L. Pan, Multi-role TiO_2 layer coated carbon@few-layered MoS_2 nanotubes for durable lithium storage, Chem. Eng. J. 406 (2021) 126873.
[49] H. Wang, T. Yao, C. Li, L. Meng, Y. Cheng, Constructing three-dimensional ordered porous MoS_2/C hierarchies for excellent high-rate long-life pseudocapacitive sodium storage, Chem. Eng. J. 397 (2020) 125385.
[50] W. Wu, J. Wang, Q. Deng, H. Luo, Y. Li, M. Wei, Low crystalline 1T-MoS_2@S-doped carbon hollow spheres as an anode material for Lithium-ion battery, J. Colloid Interface Sci. 601 (2021) 411-417.